Chemical Engineering Journal 159 (2010) 138–148

Contents lists available at ScienceDirect

Chemical Engineering Journal

journal homepage: www.elsevier.com/locate/cej

Gas–solid flow hydrodynamics of an industrial scale catalyst lift engager

Milinkumar T. Shah[a], Jeff Mayne[b], Ranjeet P. Utikar[a], Moses O. Tade[a], Vishnu K. Pareek[a,*]

[a] Department of Chemical Engineering, Curtin University of Technology, GPO Box U1987, Perth, Western Australia 6845, Australia
[b] BP Kwinana Refinery Pty Ltd., Mason Road, Kwinana, Western Australia 6167, Australia

ARTICLE INFO

Article history:
Received 18 September 2009
Received in revised form 25 January 2010
Accepted 28 January 2010

Keywords:
Lift engager
Gas–solid flow modelling
Eulerian–Eulerian approach
Drag
Frictional pressure

ABSTRACT

This study characterizes the hydrodynamics of an industrial scale lift engager which circulates the catalyst between the reactor and regenerator sections of a continuous catalytic reformer in an oil refinery. The flow of Geldart D particles in this unit was simulated using a granular Eulerian model. Before studying the influence of the operating parameters, the effect of several model parameters such as the drag and the frictional pressure models on the predictions was carried out. Whilst all of the drag models investigated in this study (Gidaspow and Syamlal–O'Brien models) gave qualitatively similar results, the choice of the frictional pressure model affected the simulation results in a rather astounding manner. The KTGF based frictional pressure model gave inconsistent results as both catalyst velocity and its volume fraction increased along the lift line. However, the Johnson and Jackson model overcame this drawback. Interestingly, both KTGF based and Johnson and Jackson models gave similar results for the flow inside a simple riser. Therefore, it can be concluded that for complex flow domains having both dilute and dense phase flows, the most widely used KTGF model may not be appropriate and Johnson and Jackson model should be used instead. After optimizing the selection of model parameters, simulations were conducted to study the effect of the lift gas velocity. It was observed that a lower lift gas velocity leads to large-scale fluctuations in the outlet mass flow rate. The simulation results were also compared with the previously reported studies on the riser flow with a reasonable qualitative agreement.

1. Introduction

Catalytic reforming is a process of great interest to petroleum refinery and petrochemical industry for the production of aromatic compounds which are raw materials for several petrochemical products and gasoline additives. Typically, the reforming units are of two types; semi-regenerative reforming (SSR) unit (older) and continuous catalyst regeneration reforming (CCR) (newer) unit, which is characterized by an in-situ regeneration of the catalyst.

A schematic diagram of a lift engager and catalyst circulation circuit of CCR is shown in Fig. 1. The lift engagers (LE1 and LE2) shown in Fig. 1 hold, fluidize and transport the catalyst between the reaction and regeneration zones of the CCR. Typically, the recycled hydrocarbon gas and hydrogen are used as the lifting fluid. The spent catalyst flows from the bottom of the last stacked reactor bed through a lock hopper to a lift engager. The circulating lift gas enters through two inlets, namely, primary and secondary inlets and lifts the catalyst through a lift pipe to a disengaging hopper located above the regeneration tower. The catalyst is then fed to the regeneration tower from the bottom of the disengaging hopper. The regenerated catalyst follows a similar circuit and is transported to the reactor through another lift engager situated at the bottom of the regenerator. A typical lift engager is a cylindrical vessel with two concentric pipes, a catalyst inlet dip and a secondary gas inlet line (see inset Fig. 1). The lift gas enters as two separate gas streams called the primary and secondary gas streams. The primary gas enters from the annular space between the two concentric pipes and the secondary gas enters separately from a side inlet. The secondary gas travels over a flow restricting baffle to the main body of the lift engager. The lifted catalyst is discharged through the extended centre pipe called the lift line.

One of the key aspects of the CCR is the catalyst circulation between the reactor and regenerator. It is important to maintain a sufficient rate of circulations as inefficient catalyst circulations may lead to retardation of reforming reaction rate. Generally, to compensate for the reduced reaction rate, make up catalyst must be added which affects the economy of the whole plant. The catalyst circulation is controlled by the lift engagers situated at the bottom of the reactor and regenerator. The efficiency of the lift engager in terms of catalyst lift rate depends on various operating and design parameters such as the lift gas velocity, lift line gap and catalyst feed rate. The hydrodynamics of the gas solid flow plays an important role in governing the performance of the lift engager. Higher gas velocities in the lift line can result in excessive catalyst attrition, whereas low gas velocities can produce an unstable lifting. In this

* Corresponding author. Tel.: +61 8 9266 4687; fax: +61 8 9266 2681.
E-mail address: v.pareek@curtin.edu.au (V.K. Pareek).

1385-8947/$ – see front matter © 2010 Elsevier B.V. All rights reserved.
doi:10.1016/j.cej.2010.01.055

Nomenclature

d	solid diameter (m)
e_{ss}	coefficient of restitution
F_r	empirical material constant (kg m^2 s^{-2})
g	gravitational acceleration (m s^{-2})
$g_{o,ss}$	radial distribution function
I	unit stress tensor
I_{2D}	second invariant of the deviatoric stress tensor
K	momentum exchange coefficient (dimensionless)
n	empirical material constant in frictional pressure model
p	empirical material constant in frictional pressure model
p	pressure (kg m^{-1} s^{-2})
P_s	solids pressure (kg m^{-1} s^{-2})
P_f	frictional pressure (kg m^{-1} s^{-2})
Re_s	particle Reynolds number
t	time (s)
v	velocity (m s^{-1})
$V_{r,s}$	ratio of the terminal velocity of multiparticle system to that of an isolated particle
Z^*	dimensionless height of the lift line

Greek letters

α	volume fraction
ρ	density (kg m^{-3})
τ	stress tensor (kg m^{-1} s^{-2})
μ_g	gas viscosity (kg m^{-1} s^{-1})
μ_s	solid viscosity (kg m^{-1} s^{-1})
λ_s	solid bulk viscosity (kg m^{-1} s^{-1})
Θ_s	granular temperature (m^2 s^{-2})
ϕ	angle of internal friction

Subscripts

Col	collisional
kin	kinetic
fri	frictional
f	frictional
max	maximum
min	minimum
g	gas phase
s	solid phase

Abbreviation

CCR	Continuous catalytic reforming
CFD	Computational fluid dynamics
DEM	Discrete element model
KTGF	Kinetic theory of granular flows
LE	Lift engager
QUICK	Quadratic upstream interpolation for convective kinetics
SIMPLE	Semi-implicit method for pressure-linked equations

study, the hydrodynamics of a lift engager has been characterized using a granular Eulerian–Eulerian model.

2. Hydrodynamic modelling of gas–solid flows

Recently, computational fluid dynamics (CFD) simulations have been extensively used to study the hydrodynamics of gas–solid flows (Huilin et al. [1], Utikar and Ranade [2], Sarkar et al. [3] and Geng et al. [4]). The classification, structure and applicability of these CFD models have been discussed in detail by Van der Hoef et al. [5] and van Wachem et al. [6]. Based on the treatment of the solid phase, the CFD models can be primarily divided into two categories, namely, the Eulerian–Lagrangian and the Eulerian–Eulerian approaches. In the Eulerian–Lagrangian approach, the gas phase is continuous and the solid phase is represented as a collection of discrete particles that obey the second law of Newton. The accuracy of simulation in the Eulerian–Lagrangian model is dependent on the number of particles tracked, which in turn is dependent on the computational resources employed. Therefore, for realistic industrial scale simulations, this approach is computationally intensive. In the Eulerian–Eulerian model, both the solid and gas phases are represented as continuous and interpenetrating. This representation is computationally less intensive and is well suited for modelling of industrial scale flows [7].

In the Eulerian–Eulerian model, basic transport equations in terms of mass and momentum conservation are written for each phase using an averaging. Enwald et al. [8] have discussed various averaging techniques for the formulation of the two-fluid model equations. The ensemble averaging of local instantaneous balances for each phase is used in formulating the averaged governing equations that are used in the CFD code such as FLUENT (Fluent 2008). For each phase, the continuity and momentum balance equations are written.

2.1. Continuity equation

The continuity equation for the gas may be written as:

$$\frac{\partial}{\partial t}(\alpha_g \rho_g) + \nabla \cdot (\alpha_g \rho_g \vec{v}_g) = 0 \quad (1)$$

and that for the solid as:

$$\frac{\partial}{\partial t}(\alpha_s \rho_s) + \nabla \cdot (\alpha_s \rho_s \vec{v}_s) = 0 \quad (2)$$

The continuity equation represents the mass of balance for a phase and is solved for each of the primary phases. Additionally, the constraint on the volume fractions prescribes the sum of volume fraction of each phase should be equal to one.

2.2. Momentum conservation equation

The conservation of momentum for the gas and the solid phase is given by Eqs. (3) and (4) respectively:

$$\frac{\partial}{\partial t}(\alpha_g \rho_g \vec{v}_g) + \nabla \cdot (\alpha_g \rho_g \vec{v}_g \vec{v}_g) = -\alpha_g \nabla p - \nabla \cdot (\overline{\overline{\tau_g}}) + \alpha_g \rho_g \vec{g} + K_{sg}(\vec{v}_g - \vec{v}_s) \quad (3)$$

$$\frac{\partial}{\partial t}(\alpha_s \rho_s \vec{v}_s) + \nabla \cdot (\alpha_s \rho_s \vec{v}_s \vec{v}_s) = -\alpha_s \nabla p - \nabla p_s - \nabla \cdot (\overline{\overline{\tau_s}}) + \alpha_s \rho_s \vec{g} + K_{gs}(\vec{v}_g - \vec{v}_s) \quad (4)$$

The momentum exchange between the two phases is based on the value of the fluid solid exchange coefficient K_{gs} (=K_{sg}).

2.3. Interphase exchange coefficient

A number of interphase exchange coefficient functions (drag models) are available in the literature for specific multiphase flow regimes. Drag models based on the pressure drop measurement, bed expansion studies and numerical experiment have been reported in the literature [9]. Two of the most commonly used drag models for gas solid flows are that of Syamlal and O'Brien [10] and Gidaspow et al. [11]. These are applicable to a wide range of particle Reynolds numbers and flow conditions.

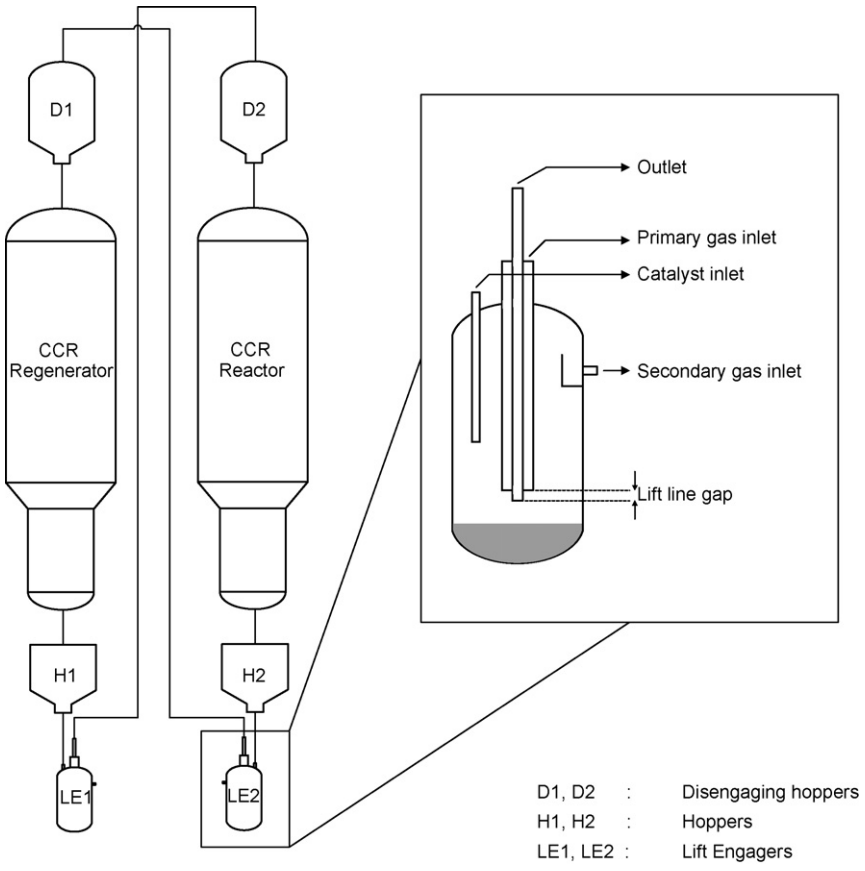

Fig. 1. Schematic diagram of catalyst circulation circuit in CCR and lift engager.

The Gidaspow drag model [11] is a combination of the Ergun equation [12] (which is based on the pressure drop in packed bed) and the Wen–Yu equation [13] (which is based on the settling of solids in liquid). For the voidage less than 0.8, the Ergun equation is applied and for the voidage greater than or equal to 0.8, Wen–Yu equation is applied. A step change in drag value is realised at the crossover. Eqs. (5)–(8) describe this model:

$$K_{gs} = 150\frac{\alpha_s^2\mu_g}{(1-\alpha_s)d_s^2} + 1.75\frac{\rho_g\alpha_s|\vec{v}_g - \vec{v}_s|}{d_s}, \quad \text{if } \alpha_g < 0.8 \quad \text{(Ergun [12])} \tag{5}$$

$$K_{gs} = \frac{3}{4}C_D\frac{\rho_g\alpha_s(1-\alpha_s)\left|\vec{v}_g - \vec{v}_s\right|}{d_s}(1-\alpha_s)^{-2.65}, \quad \text{if } \alpha_g \geq 0.8 \quad \text{(Wen and Yu [13])} \tag{6}$$

$$C_D = \frac{24}{\alpha_g\, Re_s}[1 + 0.15(\alpha_g\, Re_s)^{0.687}], \quad \text{if } \mathrm{Re}_s < 1000$$
$$= 0.44, \quad \text{if } \mathrm{Re}_s \geq 1000 \tag{7}$$

$$Re_s = \frac{d_s\rho_g\left|\vec{v}_g - \vec{v}_s\right|}{\mu_g} \tag{8}$$

The Syamlal and O'Brian drag model [10] (Eqs. (9)–(12)) is based on the velocity–voidage correlations derived using sedimentation and fluidization experiments of Richardson and Zaki [14] and Garside and Al-Dibouni [15] respectively. The drag compares well with the Ergun equation in the void fraction range of 0.5–0.6 and it correctly reduces to a single particle drag coefficient when the void fraction becomes one. The model provides for adjustable factors that can be tuned to match the minimum fluidization velocity for the solid particles in question. The following are the equations describing this model:

$$K_{gs} = \frac{3}{4}C_D\frac{\alpha_s(1-\alpha_s)\rho_g}{v_{r,s}^2 d_s}\left(\frac{Re_s}{v_{r,s}}\right)\left|\vec{v}_g - \vec{v}_s\right| \tag{9}$$

$$C_D = \left(0.63 + 4.8\sqrt{\frac{v_{r,s}}{Re_s}}\right)^2 \tag{10}$$

$$v_{r,s} = \frac{1}{2}\left[A - 0.06Re_s + \sqrt{(0.06Re_s)^2 + 0.12Re_s(2B - A) + A^2}\right] \tag{11}$$

$$A = (1-\alpha_s)^{4.14}$$
$$B = 0.827(1-\alpha_s)^{1.28} \quad \text{if } \alpha_s \geq 0.15$$
$$= (1-\alpha_s)^{2.44} \quad \text{if } \alpha_s < 0.15 \tag{12}$$

The drag coefficient (C_D) mainly depends on the voidage (α_s), particle diameter (d_s), the difference between fluid and solid phase velocities ($v_g - v_s$) and particle Reynolds number (Re_s).

2.4. Phase stress–strain tensors

The stress strain tensors for gas and solid phase are given by Eqs. (13) and (14) respectively:

$$\bar{\bar{\tau}}_g = \mu_g(\nabla\vec{v}_g + \nabla\vec{v}_g^T) + \left(\lambda_g - \frac{2}{3}\mu_g\right)\nabla\vec{v}_g\bar{\bar{I}} \tag{13}$$

$$\alpha_s\bar{\bar{\tau}}_s = -P_s\bar{\bar{I}} + \mu_s\alpha_s(\nabla\vec{v}_s + \nabla\vec{v}_s^T) + \left(\lambda_s - \frac{2}{3}\mu_s\right)\nabla\vec{v}_s\bar{\bar{I}} \tag{14}$$

The solid phase stress tensor has additional terms arising from the continuum assumption of the discrete granular phase. The solid

phase stresses, are derived by making an analogy between the random particle motion and the thermal motion of gas molecules; the kinetic theory of granular flows (KTGF). Unlike the gas kinetic theory, the KTGF model accounts for the inelasticity of particle–particle collision. The intensity of the particle velocity fluctuations determines the stresses, viscosity and pressure of the solid phase. The kinetic energy associated with the particle velocity fluctuations is represented by a granular temperature (Θ_s) which is proportional to the mean square of the random motion of the particle.

$$\Theta_s = \frac{1}{3}\overline{v_s^2} \tag{15}$$

Various correlations have been proposed in the literature for the solid phase transport closures (equations for solid viscosity, radial distribution function, solids pressure). A comparative study of these relations was presented by van Wachem et al. [16] and Ahuja and Patwardhan [17].

The solids pressure (P_s) represents the normal solid phase forces due to particle–particle interactions. It is calculated independently and used for the pressure gradient term in the phase stress tensor. The solids pressure is composed of a kinetic term and a second term due to the particle collisions. The solids bulk viscosity (λ_s) is the resistance of particle suspension against the compression. For solids pressure and solid bulk viscosity, there is a general agreement in the literature on the relation proposed by Lun et al. [18]. The solid shear viscosity (μ_s) (given by Eq. (18)) is made up of the collisional, frictional and kinetic parts. All the models for solid shear viscosity yield practically the same solid shear viscosity at solid volume fraction greater than 0.25. For the lower volume factions, the models start deviating from one another [17]. However, there are no clear guidelines on selecting the solid shear viscosity model. The Gidaspow model [19] for the solid shear viscosity neglects the inelastic nature of particle collisions in the kinetic contribution of the total stress and was used in this study. The frictional viscosity was calculated using Schaeffer's model. The model equations used in the present study are listed below (Eqs. (16)–(21)):

$$P_s = \alpha_s\rho_s\Theta_s(1 + 2(1 + e_{ss})\alpha_s g_{o,ss}) \tag{16}$$

$$\lambda_s = \frac{4}{3}\alpha_s^2\rho_s d_s g_{o,ss}(1 + e_{ss})\sqrt{\frac{\Theta}{\pi}} \tag{17}$$

$$\mu_s = \mu_{s,col} + \mu_{s,kin} + \mu_{s,fri} \tag{18}$$

$$\mu_{s,col} = \frac{4}{5}\alpha_s^2\rho_s d_s g_{o,ss}(1 + e_{ss})\sqrt{\frac{\Theta}{\pi}} \quad \text{(Giaspown model [19])} \tag{19}$$

$$\mu_{s,kin} = \frac{10\rho_s d_s\sqrt{\Theta\pi}}{96\alpha_s(1 + e_{ss})g_{o,ss}}\left[1 + \frac{4}{5}\alpha_s^2 g_{o,ss}(1 + e_{ss})\right]^2$$
(Gidaspow model [19]) (20)

$$\mu_{s,fri} = \frac{p_s \sin\phi}{2\sqrt{I_{2D}}} \quad \text{(Schaeffer model [20])} \tag{21}$$

where e_{ss} is the coefficient of restitution, which determines the degree of elasticity of particle–particle collisions. For typical gas–solid applications, the restitution coefficient has a value between 0.7 and 0.95. I_{2D} is the second invariant of the deviatoric stress tensor and ϕ is an angle of internal friction. P_s is the frictional solid pressure which accounts for the solid pressure in the frictional regime. The default frictional pressure model which is based on the KTGF as well as the model of Johnson and Jackson [21] was applied in this work. $g_{o,ss}$ is the radial distribution function, which is a correction factor that modifies the probability of collisions between particles when the granular phase becomes dense. Comparative studies show only a little difference between various models for the radial distribution function at different solid volume fractions. In this work, the model proposed by Lun et al. [18] (Eq. (22)) was used for the radial distribution function.

Johnson and Jackson [21] frictional pressure model:

$$p_f = F_r\frac{(\alpha_s - \alpha_{s,\min})^n}{(\alpha_{s,\max} - \alpha_s)^p} \tag{22}$$

where F_r, n and p are empirical material constants and $\alpha_{s,\min}$ is the critical value of solid volume fraction when frictional stresses become important.

Radial distribution function (Lun et al. [18]):

$$g_{o,ss} = \left[1 - \frac{\alpha_s}{\alpha_{s,\max}}\right]^{-2.5\alpha_{s,\max}} \tag{23}$$

3. CFD simulation

The Eulerian–Eulerian gas–solid flow model in FLUENT was used for simulating an industrial scale 3D lift engager which was meshed using GAMBIT as shown in Fig. 2a. Most of the flow domain was meshed using structured hexahedral-cooper grid scheme with unstructured tetrahedral meshing in other parts. Transient CFD simulations were carried out with a time step of 1×10^{-4} and approximately 435,000 grid points on a cluster of eight processor machines. A second order discretisation scheme was used for the momentum equation and the QUICK scheme was applied to solve the volume fraction. The pressure–velocity coupling was resolved using the SIMPLE algorithm. The turbulence in gas phase was modelled using the standard k–ε approach. A set of closure equations for the Eulerian–Eulerian model used in the current study are described in the previous section and also summarized in Table 1. The lift gas (a mixture of hydrocarbons) and catalyst were used as

Table 1
CFD simulation parameters used in this study.

Phase properties	
Gas phase (hydrocarbon gas)	
Density	0.889 kg m^{-3}
Viscosity	1.15×10^{-5} kg m^{-1} s^{-1}
Solid phase (reforming catalyst)	
Bulk density	933 kg m^{-3}
Particle size	1.6 mm
Modelling parameters	
Gas phase (Eulerian approach)	
Turbulence	k–ε model
Solid phase (Eulerian approach)	
Shear viscosity	Gidaspow et al.
Bulk viscosity	Lun et al.
Frictional viscosity	Schaeffer
Frictional pressure	Johnson and Jackson
Granular temperature	Lun et al.
Radial distribution function	Lun et al.
Solid pressure	Lun et al.
Drag model	Gidaspow et al. Syamlal and O'Brien
Maximum packing limit	0.63
Restitution coefficient	0.9
Angle of internal friction	30°
Simulation parameters	
Number of mesh volumes	434,966
Average grid size	0.8359 cm^3
Time step size	0.0001 s
Discretisation	Second order
Pressure–velocity coupling algorithm	SIMPLE

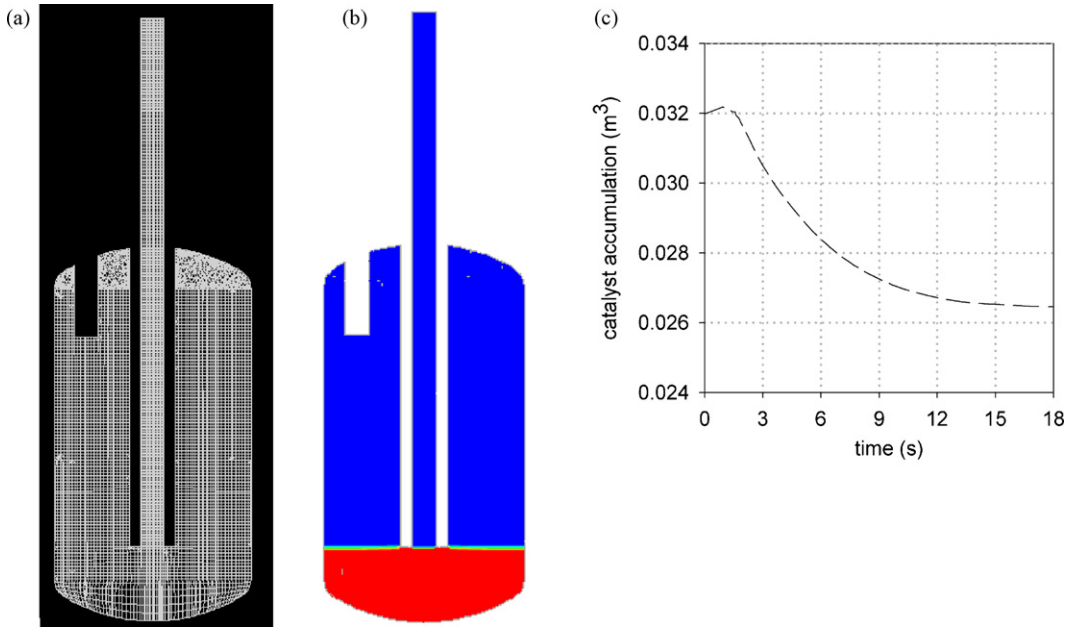

Fig. 2. (a) Grid design. (b) Initial catalyst accumulation inside the lift engager. (c) Change in catalyst accumulation as a function of time (catalyst flow rate = 0.19 kg s^{-1}, primary gas = 5 m s^{-1}, secondary gas velocity = 7 m s^{-1}).

the gas and solid phases respectively. Physical properties of both phases are given in Table 1.

Velocity-inlet boundary conditions were used for all inlets streams (solid, primary gas and secondary gas inlets). Simulations were performed for a constant catalyst flow rate of 0.19 kg s^{-1} for various flow rates for the primary and secondary gases. The operating pressure was set to 6.3×10^5 kPa. The interaction between the solids and the wall can be modelled as no-slip, free-slip or boundary condition based on the momentum transfer by collisions of particles with the wall [21]. The preliminary computations showed a little sensitivity to the wall boundary conditions for this geometry. Therefore, for all subsequent simulations, the walls were assumed with no-slip conditions. Finally, a pressure outlet boundary condition was applied for the outlet.

4. Results and discussion

The initial catalyst bed was patched with packed solids (volume fraction 0.63) up to the entrance of the lift line as shown in Fig. 2b and simulations were commenced in an unsteady manner. As shown in Fig. 2c, the total catalyst accumulation in the equipment gradually depleted during the course of simulation before stabilising. It is clear that it took about 15 s or more for the system to come to a dynamic steady-state in terms of catalyst inventory. Even after this period the mass flow rate of solids at the outlet continuously fluctuated albeit with much smaller amplitudes with its time-averaged value being approximately equal to the inlet mass flow rate. The unsteady time-averaged statistics for the catalyst velocity, catalyst volume fraction and the slip velocity, discussed below were collected after this initial period (i.e. after 15 s or more).

Initial numerical experiments were carried out to evaluate the effect of the grid size by conducting simulations on the lift engager with three different grid densities with average cell sizes being approximately 1.6914 cm^3, 0.8359 cm^3 and 0.6010 cm^3 (190,000, 435,000 and 530,000 grid points) respectively. Fig. 3 shows the calculated pressure at the outlet as a function of time. It is clear that the behaviour for the first coarser grid was substantially different from the other two finer grids. Since there was minimal refinement in results with reducing the grid size from 0.8359 cm^3 to 0.6010 cm^3, a grid size of 0.8359 cm^3 was used for the remaining of the simulations in this study.

Fig. 4 shows the snapshots of catalyst volume fraction contour and catalyst velocity vectors on axis plane, path lines of gas phase entering from primary and secondary gas inlets for the base case simulation. It was observed that the catalyst falls though the inlet with an increasing velocity and decreasing volume fraction under the effect of gravity and the convective effect of the secondary gas (Fig. 4a and b). The secondary gas velocity reduces considerably after passing through the baffle region due to the sudden increase in the cross sectional area (Fig. 4c). It appeared that the recommended secondary gas velocity was not adequate to fully fluidize the catalyst, therefore, resulting in a very poor mixing. Similarly, the primary gas immediately changed its direction upwards after entering the vessel and thus lifting the catalyst in the lift line although without any interaction with the bulk of solids in the equipment (Fig. 4c).

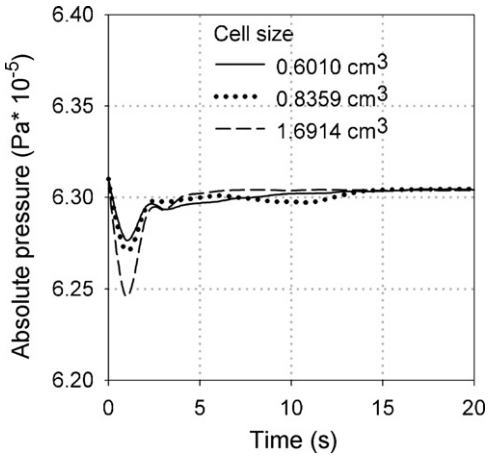

Fig. 3. Effect of grid size (catalyst flow rate = 0.19 kg s^{-1}, primary gas = 5 m s^{-1}, secondary gas velocity = 7 m s^{-1}).

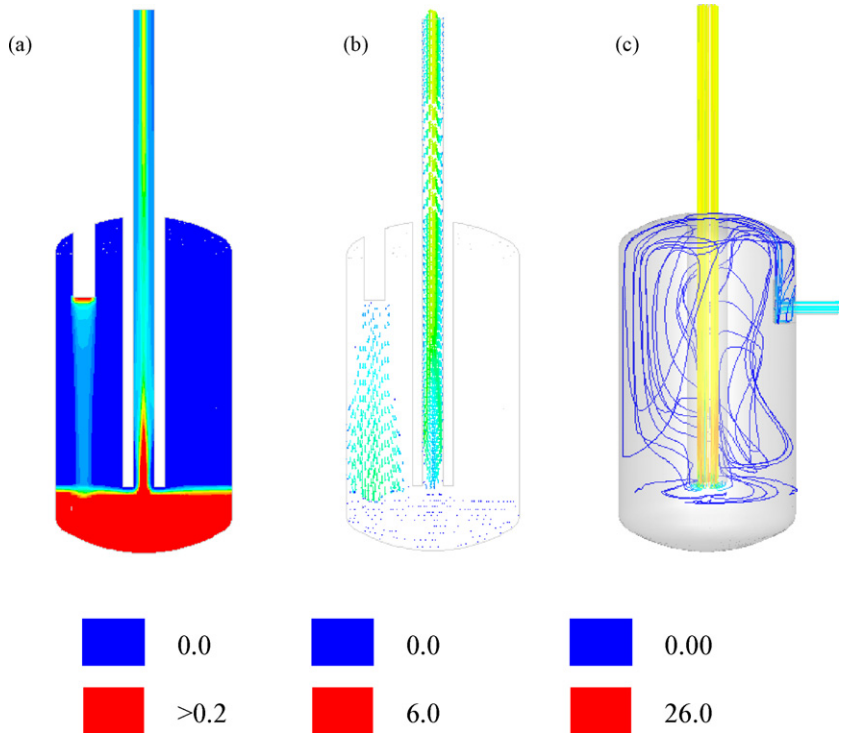

Fig. 4. Snap shots of (a) catalyst volume fraction contour; (b) catalyst velocity vectors; and (c) path lines of the lift gas entering from primary and secondary gas inlets (catalyst flow rate = 0.19 kg s^{-1}, primary gas = 5 m s^{-1}, secondary gas velocity = 7 m s^{-1}).

4.1. Effect of drag models

Most gas–solid drag models are based on the empirical co-relations derived from physical or numerical experiments. Although, the drag models for the multiphase systems have been studied extensively, there are no clear guidelines for the selection of an appropriate drag model applicable specific to a particular system. This selection is primarily based on the granular flow regime and particles Reynolds numbers in the flow domain. However, the gas–solid flow in the lift engager can be characterized by the existence of multiple granular flow regimes in the different parts of the system with the bulk of the lift engager being in dense and the lift line exhibiting dilute gas–solid flow regime. Therefore, in this study, two drag models namely, Gidaspow [11] and Syamlal and O'Brien [10], which are applicable for a wide range of particle Reynolds numbers and flow conditions were selected for comparative analysis. To study the effect of drag models on the flow predictions for both the dense and the dilute flows, the simulation results at three locations with two being in the lift line and one at the top of the catalyst bed were compared. The comparison of the time-averaged radial profiles of the catalyst velocity and volume fraction at the selected locations is shown in Fig. 5. The comparison revealed considerable differences in the values of the catalyst velocity and volume fraction calculated by the two drag models.

The Syamlal and O'Brien drag model [10] always predicted higher catalyst velocities than the Gidaspow drag model [11] (Fig. 5a, c and e). The Gidaspow drag model calculated high volume fractions than the Syamlal and O'Brien drag model for the dilute flow in the lift line (Fig. 5b and d). But in the dense catalyst bed, both drag models predicted same catalyst volume fraction (Fig. 5f). It was also observed that both the catalyst velocity and volume fraction profiles in the lift line are parabolic with the lower values near the wall. The increasing catalyst velocity along the height of the lift line suggests that the flow is dominated by the drag force over the gravitational force in the lift line. However, in the catalyst bed region, there is no observable movement of the catalyst indicating the dominance of the frictional force over the interphase exchange drag force.

From the above observations, it can be concluded that the selection of the drag model can have significant effect on the simulation results. Hence, experimental observations should be considered to justify the selection of a drag model. However in absence of the relevant experimental data, the previously published literatures on gas–solid flow modelling of similar applications such as the spouted bed and the pneumatic conveying with comparable solid phase properties can provide useful ground for the selection of the drag model. Table 2 lists the selection criteria for drag models from the applications similar to the lift engager. Based on this criterion, the Gidaspow model, which had been applied in most of the previous studies with coarse particle, was selected for all successive simulations.

Table 2
Selection of drag model for lift engager.

	Author	Application	Model	Particle diameter (mm)	Density (kg m^{-3})	Drag model
1	Sakai and Koshizuka [22]	Pneumatic conveying	DEM	1	1000	Ergun
2	Levy [23]	Pneumatic conveying	Eulerian–Eulerian	3	880	Gidaspow
3	Duarte et al. [24]	Spouted bed	Eulerian–Eulerian	6	1173	Gidaspow
4	Kawaguchi et al. [25]	Spouted bed	DEM	3	2500	Gidaspow
5	Gryczka et al. [26]	Spouted bed	Eulerian–Eulerian	1.75	1040	Gidaspow
6	Du et al. [27]	Spouted bed	Eulerian–Eulerian	1.41	2500	Gidaspow

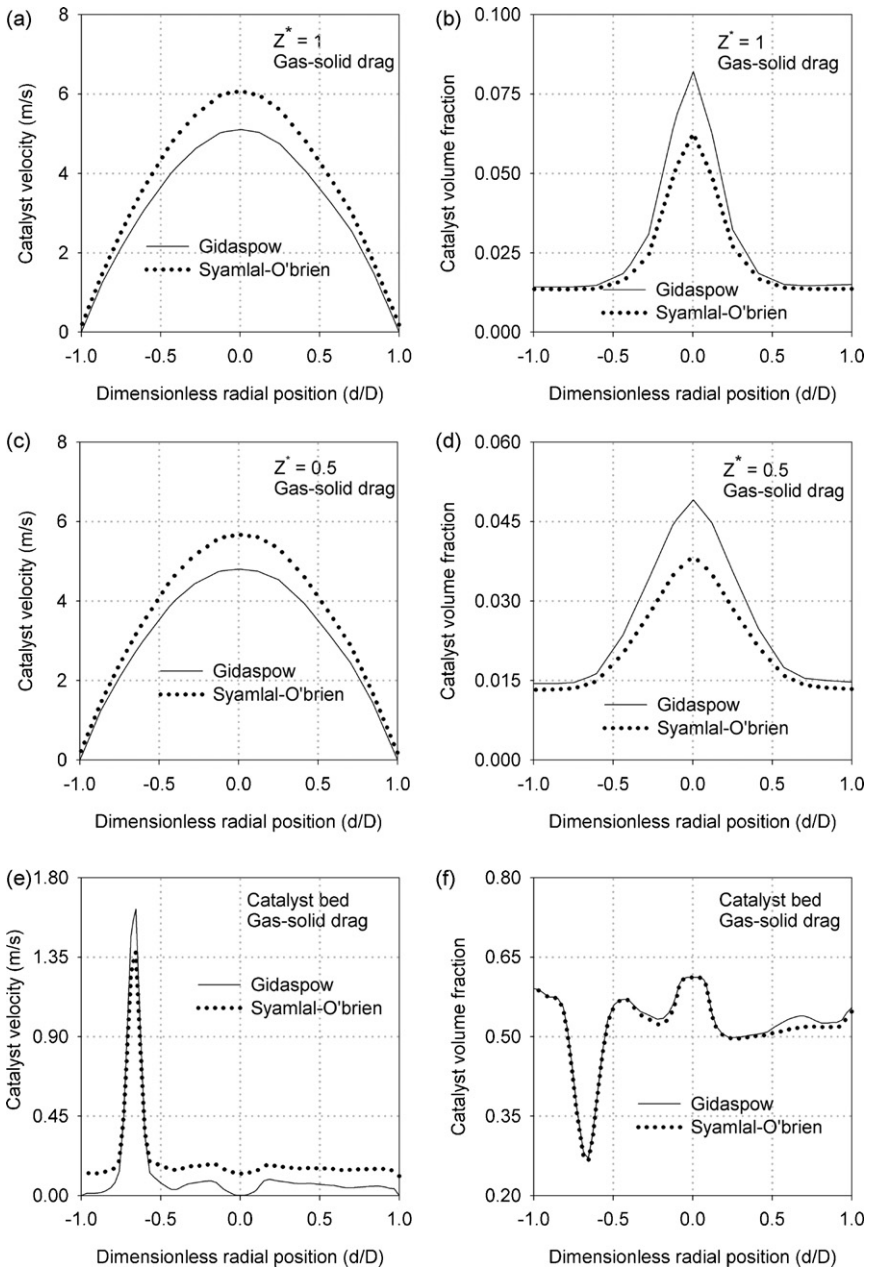

Fig. 5. Time-averaged radial profiles of (a) catalyst velocity at top of the lift line; (b) catalyst volume fraction at top of the lift line; (c) catalyst velocity at middle of the lift line; (d) catalyst volume fraction at middle of the lift line; (e) catalyst velocity at top of the catalyst bed; (f) catalyst volume fraction at top of the catalyst bed (catalyst flow rate = 0.19 kg s^{-1}, primary gas = 5 m s^{-1}, secondary gas = 7 m s^{-1}).

4.2. Effect of frictional pressure

The stress tensor appearing in the momentum balance equation for the granular phase includes the viscosity terms for kinetic/collision and frictional flow regime. The frictional viscosity becomes dominant when the solid phase volume fraction nears the maximum packing limit. The effect of frictional viscosity is significant in applications such as fluidized bed and the spouted bed. Whereas the frictional viscosity can be neglected for the dilute flows appeared in the riser application. As shown in Fig. 6e, the catalyst bed at the bottom of the lift engager has volume fraction close to the maximum packing limit. Therefore, unlike the dilute flows in the riser, the frictional viscosity in the lift engager cannot be ignored. In this study, the frictional viscosity was accounted for using the Schaeffer model [20]. The Schaffer model also includes a frictional pressure term which can been modelled using (i) Johnson and Jackson [21], (ii) Syamlal [28] and (iii) the KTGF based models. According to van Wachem et al. [16], the frictional stress calculated by Johnson and Jackson and Syamlal model can differ by orders of magnitude. In the KTGF based approach, the solid pressure calculated using the granular kinetic theory (Fluent user guide).

A comparison between simulation results for the lift engager using Johnson and Jackson and the KTGF based model is shown in Fig. 6. For the KTGF model, the catalyst volume fraction near the entrance of the lift line was observed to be almost zero and it increased along the height of the lift line (Fig. 6a). Whereas, the Johnson and Jackson model predicted higher catalyst volume fraction near the entrance that reduced along the axial height of the lift line (Fig. 6b). The time-averaged catalyst velocity and volume fraction profiles along the lift line were also compared and shown in Fig. 6c and d. It can be seen that for the KTGF model, both catalyst velocity and volume fraction increased along the height of

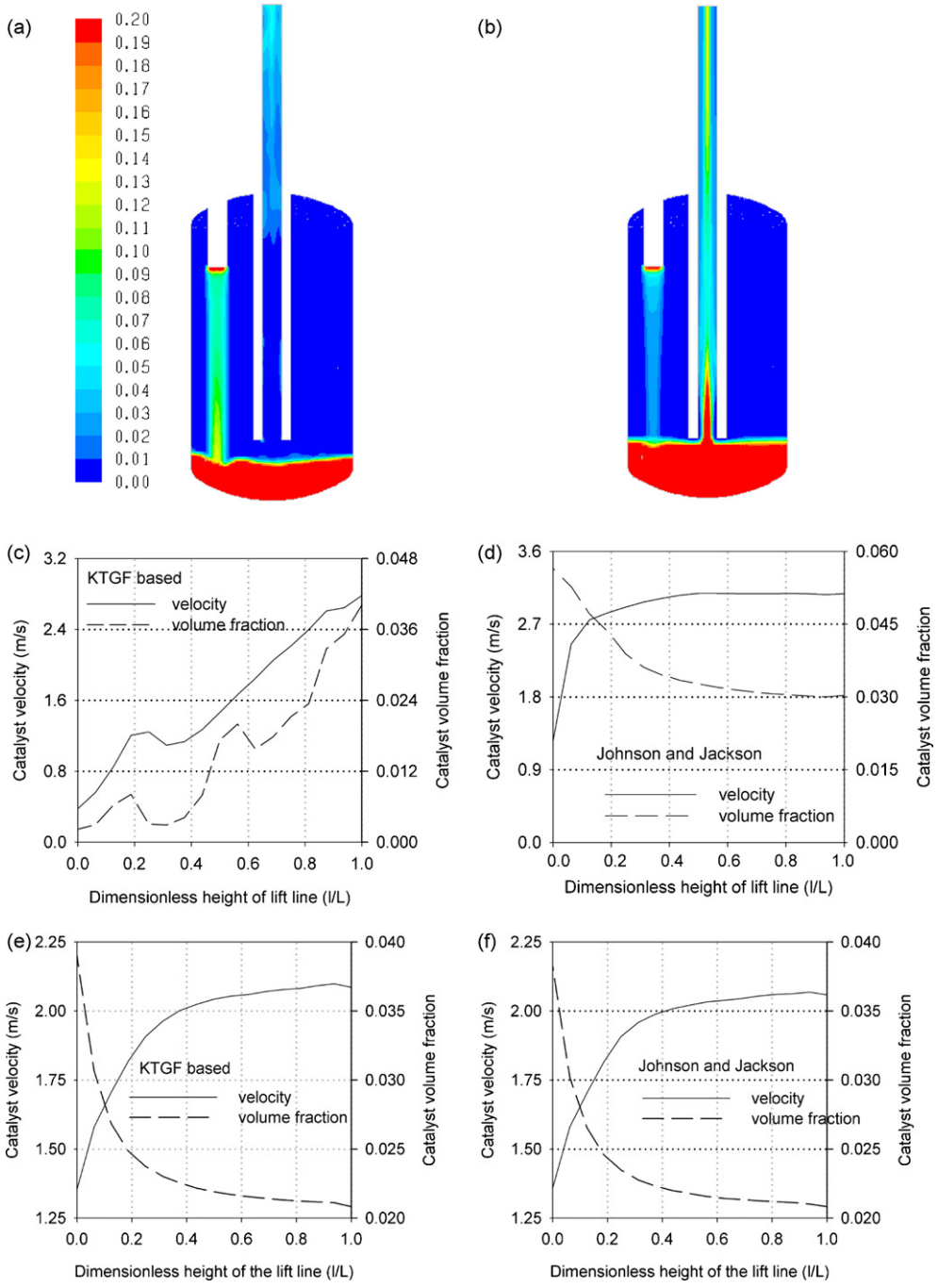

Fig. 6. Effect of the frictional pressure model: (a and b) contour of catalyst volume fraction for KTGF based and Johnson and Jackson approach respectively; (c and d) catalyst velocity and volume fraction profiles for KTGF based and Johnson and Jackson approach respectively (catalyst flow rate = 0.19 kg s^{-1}, primary gas = 5 m s^{-1}, secondary gas = 7 m s^{-1}); (e) catalyst velocity and volume fraction profiles for riser simulation with KTGF based model; (f) catalyst velocity and volume fraction profiles for riser simulation with Johnson and Jackson model.

the lift line for a constant mass flow rate at the inlet. This prediction is illogical since it violates the fundamental principle of mass conservation. However, the profiles for Johnson and Jackson model overcame this drawback where the velocity increased and the volume fraction decreased along the axial height of the lift line. These results are consistent with the previously published data for vertical pneumatic conveying systems (Theologos and Markatos [29], Arastoopour and Gidaspow [30] and Littman et al. [31]).

It is worth noting that the above drawback in the KTGF based frictional pressure model has not been reported previously because most of the previously reported simulations are for a relatively simple geometry of risers. In order to evaluate the possible reasons for the discrepancy in Fig. 6c, simulations were conducted inside a simple riser (having the same diameter as the lift line in Fig. 2) with the same particle properties. As shown in Fig. 6e and f, both KTGF based model and Johnson and Jackson model gave very similar results for the flow inside the riser. Hence, it can be concluded that the KTGF based frictional pressure model can be useful for the flow inside simple geometries, but for the complex granular flow systems such as that in the lift engager which involves a transition from the dense fluidization to dilute vertical pneumatic transport, the Johnson and Jackson model for the frictional pressure is more appropriate.

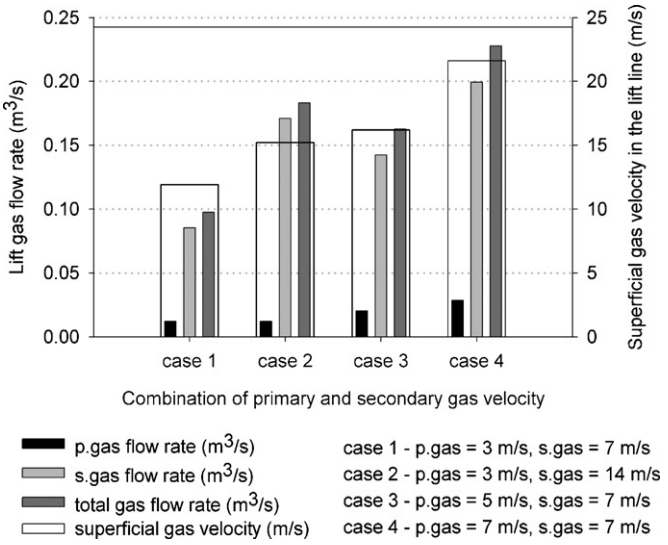

Fig. 7. Simulated combinations of primary and secondary gas velocities.

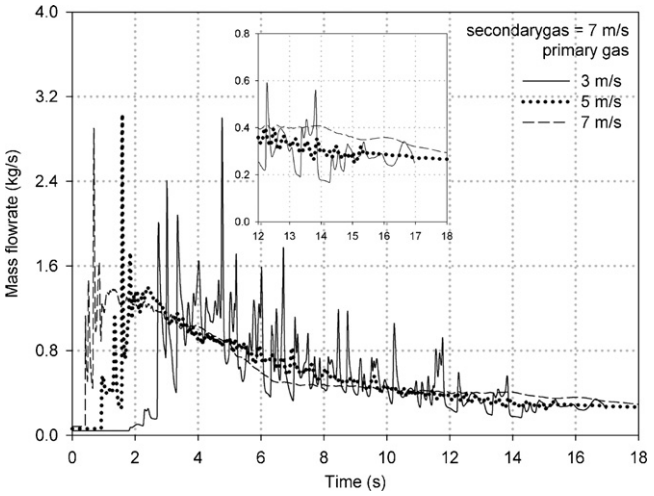

Fig. 8. Total mass flow rate at outlet as a function of time (catalyst flow rate = 0.19 kg s^{-1}).

4.3. Effect of lift gas velocity

The primary and secondary lift gas velocities are very critical parameters which not only affect the catalyst lift rate but also associated disturbances therein. To study the effect of the lift gas flow rate on the catalyst transportation in the lift line, the simulations with various flow rates of primary and secondary gases were conducted. The simulated lift gas velocities, flow rate and the resulting superficial gas velocity in the lift line are shown in Fig. 7. The mass flow rate at the outlet, the time-averaged catalyst velocity, volume fraction and slip velocity in lift line were calculated and compared.

Fig. 8 shows the total mass flow rate at outlet as a function of time for a fixed secondary gas velocity (7 m s^{-1}) and 3 different primary gas velocities. It is clear that for approximately 15 s, depending upon the primary gas velocity, there were significant fluctuations in the outlet mass flow rate surging as high as 3 kg s^{-1}. After this period, the catalyst bed height and the catalyst accumulation reached a dynamic steady-state where the mass flow rate fluctuated around an averaged value equal to the inlet mass flow rate. Although similar trends were observed for all three primary

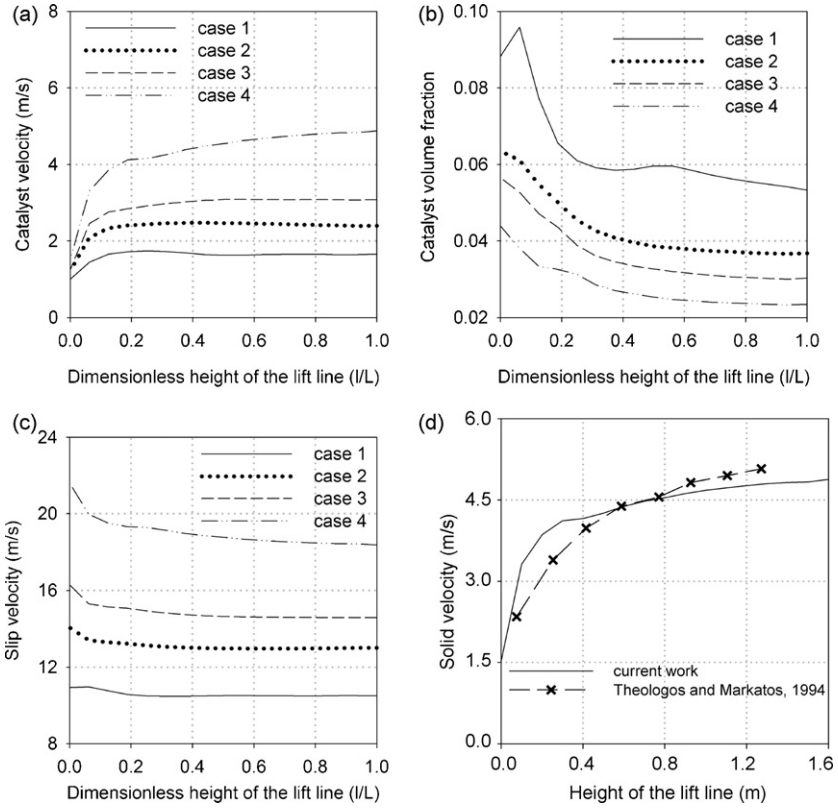

Fig. 9. Time-averaged profiles along the height of the lift line: (a) catalyst velocity; (b) catalyst volume fraction; (c) slip velocity (catalyst flow rate = 0.19 kg s^{-1}); (d) comparison between current simulation results with previously published simulation results (Theologos and Markatos; particle diameter = 0.503 mm, particle density = 2643 kg m^{-3}, riser diameter = 13.5 mm, riser height = 1.368 m, superficial velocity of air = 12.3 m s^{-1}).

gas velocities, there were considerable differences in the amplitude of fluctuations. For the primary gas velocity of 3 m s^{-1}, there existed both small and large-scale fluctuations before achieving the dynamic steady-state. For this primary gas velocity (3 m s^{-1}), as shown in the inset in Fig. 8, even after achieving the dynamic steady-state, the small-scale fluctuations in the outlet mass flow rate persisted. However, for the higher value of primary gas velocity (e.g., 7 m s^{-1}), except for a couple of high amplitude oscillations in the first 2 s, the predicted outlet mass flow rate was relatively free of small-scale fluctuations. For the primary gas velocity of 5 m s^{-1}, the fluctuations in the outlet mass flow rate could be characterized to be an average of those for 3 m s^{-1} and 7 m s^{-1}. Therefore, if smooth lifting is required, a higher flow rate of the primary lift gas is recommended. However, excessively high velocities may enhance the possibility of associated erosions, it is apparent that a primary gas velocity of 5 m s^{-1} will be optimal for the current system.

Fig. 9 shows a comparison between the time-averaged catalyst velocity, catalyst volume fraction and slip velocity profiles along the height of the lift line for 4 different cases as described in Fig. 7. Depending on the lift gas velocities, the catalyst velocity increased sharply for the initial 20–40% of the lift line. After this initial acceleration phase, the catalyst velocity became constant as it travelled upwards (Fig. 9a). As expected, an increase in the primary gas velocity increased the catalyst velocity in the lift line (compare case 3 and case 4). A similar trend was observed for the increase in the secondary gas velocity (compare case 1 and case 2). Contrary to the catalyst velocity profiles, the catalyst volume fraction profile reduced initially and then became constant for the rest of the height of the lift line (Fig. 9b). As shown in Fig. 9c, the slip velocity profiles were found to be constant for the most part of the lift line except near the entrance. For all simulated cases, the predicted slip velocities were greater than the terminal velocity of the catalyst particle (~6.87 m s^{-1}).

The simulations results were compared with the previously published results for applications such as the spouted bed and the vertical pneumatic transportation. There is no reported study for the hydrodynamics of a lift engager, which not only has a dilute phase flow in the riser but also a dense phase flow below the lift line. With some caution, current simulations may be compared with previously reported studies on risers for which abundant data is available. In this study, we have compared the lift engager simulations with previously published studies on risers using Geldart D particles. Fig. 9d compares the calculated solid velocity and previously published simulation results of Theologos and Markatos [29] and it can be seen that our results are in good agreement with their predicted solid velocity profile.

5. Conclusions

The hydrodynamics of a lift engager, which is used in catalytic reformers, was investigated using a granular Eulerian–Eulerian model. The effects of modelling parameters such as the drag model and the frictional pressure were studied, both of which strongly influenced the simulations. Two approaches for the frictional pressure, namely the KTGF based and the Johnson and Jackson [21] were simulated to study the effect of the frictional pressure on the simulation results. For the KTGF based approach, which has been found to give satisfactory results for fully developed risers, the catalyst velocity and volume fraction profile along the height of the lift line were not consistent and violated the basic principle of mass balance. This could be attributed to the existence of both dense and dilute phase inside the lift engager. However, using Johnson and Jackson [21] frictional pressure approach this inconsistency in the simulations was removed.

A parametric study was also conducted by simulating four different cases having different combinations of the primary and secondary gas velocities. At the dynamic steady-state, the catalyst outlet mass flow rate was found to be fluctuating with the average value being around the inlet mass flow rate, with fluctuations dampening rapidly upon increasing the primary lift velocity. The time-averaged profiles of gas velocity showed that the catalyst accelerated along the height of the lift line with correspondingly decreasing volume fractions. The simulation results qualitatively compared well with the previously published simulation results for risers with a reasonable agreement.

Acknowledgement

The authors wish to acknowledge the financial support from the Australian Research Council (Grant LP0882958).

References

[1] L. Huilin, D. Gidaspow, J. Bouillard, L. Wentie, Hydrodynamic simulation of gas–solid flow in a riser using kinetic theory of granular flow, Chemical Engineering Journal 95 (2003) 1–13.
[2] R.P. Utikar, V.V. Ranade, Single jet fluidized beds: experiments and CFD simulations with glass and polypropylene particles, Chemical Engineering Science 62 (2007) 167–183.
[3] S. Sarkar, K. Mohanty, B.C. Meikap, Hydrodynamic modeling of a novel multistage gas–liquid external loop airlift reactor, Chemical Engineering Journal 145 (2008) 69–77.
[4] F. Geng, D. Xu, Z. Yuan, Y. Yan, D. Luo, H. Wang, B. Li, C. Chyang, Numerical simulation on fluidization characteristics of tobacco particles in fluidized bed dryers, Chemical Engineering Journal 150 (2009) 581–592.
[5] M.A. Van der Hoef, M. van Sint Annaland, N.G. Deen, J.A.M. Kuipers, Numerical simulation of dense gas–solid fluidized beds: a multiscale modeling strategy, Annual Review of Fluid Mechanics 70 (2008) 40–70.
[6] B.G.M. van Wachem, A.E. Almstedt, Methods for multiphase computational fluid dynamics, Chemical Engineering Journal 96 (2003) 81–98.
[7] V.V. Ranade, Computational Flow Modeling for Chemical Reactor Engineering, Academic Press, 2001.
[8] H. Enwald, E. Peirano, A.E. Almstedt, Eulerian two-phase flow theory applied to fluidization, International Journal of Multiphase Flow 22 (1996) 21–66.
[9] R. Mabrouk, J. Chaouki, C. Guy, Effective drag coefficient investigation in the acceleration zone of an upward gas–solid flow, Chemical Engineering Science 62 (2007) 318–327.
[10] M. Syamlal, T.J. O'Brien, The Derivation of a Drag Coefficient Formula from Velocity-Voidage Correlations. US Department of Energy, Office of Fossil Energy, in Technical Report, 1994.
[11] D. Gidaspow, R. Bezburuah, J. Ding, Hydrodynamics of circulating fluidized beds: kinetic theory approach, in: 7th Engineering Foundation Conference on Fluidization, CONF-920502-1, Illinois Inst. of Tech., Chicago, IL (United States), Dept. of Chemical Engineering, 1991.
[12] S. Ergun, Fluid flow through packed columns, Chemical Engineering Progress 48 (1952) 89–94.
[13] C.Y. Wen, Y.H. Yu, Mechanics of fluidization, in: Chemical Engineering Progress Symposium Series, 1966, pp. 100–111.
[14] J.F. Richardson, W.N. Zaki, Sedimentation and fluidization, Transactions of the Institution of Chemical Engineers 32 (1954) 1954.
[15] J. Garside, M.R. Al-Dibouni, Velocity–voidage relationships for fluidization and sedimentation in solid–liquid systems, Industrial and Engineering Chemistry Process Design and Development 16 (1977) 206.
[16] B.G.M. van Wachem, J.C. Schouten, C.M. Van den Bleek, R. Krishna, J.L. Sinclair, Comparative analysis of CFD models of dense gas–solid systems, AIChE Journal 47 (2001) 1035–1051.
[17] G.N. Ahuja, A.W. Patwardhan, CFD and experimental studies of solids hold-up distribution and circulation patterns in gas–solid fluidized beds, Chemical Engineering Journal 143 (2008) 147–160.
[18] C.K.K. Lun, S.B. Sevage, D.J. Jeffrey, N. Chepurniy, Kinetic theories for granular flow: inelastic particles in Couette flow and slightly inelastic particles in a general flowfield, Journal of Fluid Mechanics (1984) 223.
[19] D. Gidaspow, Multiphase Flow and Fluidization: Continuum and Kinetic Theory Descriptions, Academic Press, 1994.
[20] D.G. Schaeffer, Instability in the evolution equations describing incompressible granular flow, Journal of Differential Equations 66 (1987) 19–50.
[21] P.C. Johnson, R. Jackson, Frictionakollisional constitutive relations for granular materials, with application to plane shearing, Journal of Fluid Mechanics 176 (1987).
[22] M Sakai, S. Koshizuka, Large-scale discrete element modeling in pneumatic conveying, Chemical Engineering Science 64 (2009) 533–539.
[23] A. Levy, Two-fluid approach for plug flow simulations in horizontal pneumatic conveying, Powder Technology 112 (2001) 263–272.

[24] C.R. Duarte, M. Olazar, V.V. Murata, M.A.S. Barrozo, Numerical simulation and experimental study of fluid–particle flows in a spouted bed, Powder Technology 188 (2009) 195–205.
[25] T. Kawaguchi, M. Sakamoto, T. Tanaka, Y. Tsuji, Quasi-three-dimensional numerical simulation of spouted beds in cylinder, Powder Technology 109 (2000) 3–12.
[26] O. Gryczka, S. Heinrich, N.G. Deen, J.A.M. Kuipers, L. Mörl, U. Verlag, Three-Dimensional computational fluid dynamics modeling of a prismatic spouted bed, Chemical Engineering and Technology 32 (2009) 470–481.
[27] W. Du, X. Bao, J. Xu, W. Wei, Computational fluid dynamics (CFD) modeling of spouted bed: assessment of drag coefficient correlations, Chemical Engineering Science 61 (2006) 1401–1420.
[28] M. Syamlal, W. Rogers, T.J. O'Brien, MFIX Documentation: Theory Guide, Technical Note, DOE/METC-95/1013 (1993).
[29] K.N. Theologos, N.C. Markatos, Modelling of vertical pneumatic-conveying hydrodynamics, Applied Mathematical Modelling 18 (1994) 306–320.
[30] H. Arastoopour, D. Gidaspow, Vertical pneumatic conveying using four hydrodynamic models, Industrial and Engineering Chemistry Fundamentals 18 (1979) 123–130.
[31] H. Littman, M.H. Morgan Iii, J.D. Paccione, S.D. Jovanovic, Z.B. Grbavcic, Modeling and measurement of the effective drag coefficient in decelerating and non-accelerating turbulent gas–solids dilute phase flow of large particles in a vertical transport pipe, Powder Technology 77 (1993) 267– 283.